

*Erik Jonsson School of Engineering and Computer Science
Alan G. MacDiarmid NanoTech Institute*

***Multi-Physics Simulation of Metal Printing
at Micro/Nanoscale Using Meniscus-Confined
Electrodeposition: Effect of Nozzle Speed and Diameter***

UT Dallas Author(s):

Seyedreza Morsali, Soheil Daryadel,
Zhong Zhou, Ali Behroozfar,
Mahmoud Baniyadi, Salvador Moreno,
Dong Qian and Majid Minary-Jolandan

Rights:

©2017 American Institute of Physics. This article may be downloaded for personal use only. Any other use requires prior permission of the author and AIP Publishing.

Citation:

Morsali, S., S. Daryadel, Z. Zhou, A. Behroozfar, et al. 2017. "Multi-physics simulation of metal printing at micro/nanoscale using meniscus-confined electrodeposition: Effect of nozzle speed and diameter." *Journal of Applied Physics* 121(21), doi:10.1063/1.4984910

This document is being made freely available by the Eugene McDermott Library of the University of Texas at Dallas with permission of the copyright owner. All rights are reserved under United States copyright law unless specified otherwise.

Multi-physics simulation of metal printing at micro/nanoscale using meniscus-confined electrodeposition: Effect of nozzle speed and diameter

Seyedreza Morsali,¹ Soheil Daryadel,¹ Zhong Zhou,¹ Ali Behroozfar,¹ Mahmoud Baniasadi,¹ Salvador Moreno,¹ Dong Qian,¹ and Majid Minary-Jolandan^{1,2,a)}

¹Department of Mechanical Engineering, The University of Texas at Dallas, 800 W. Campbell Rd., Richardson, Texas 75080, USA

²Alan G. MacDiarmid NanoTech Institute, The University of Texas at Dallas, 800 W. Campbell Rd., Richardson, Texas 75080, USA

(Received 5 April 2017; accepted 21 May 2017; published online 7 June 2017)

Meniscus-confined electrodeposition (MCED) is a solution-based, room temperature process for 3D printing of metals at micro/nanoscale. In this process, a meniscus (liquid bridge or capillary) between a nozzle and a substrate governs the localized electrodeposition process, which involves multiple physics of electrodeposition, fluid dynamics, mass, and heat transfer. We have developed a multiphysics finite element (FE) model to investigate the effects of nozzle speed (v_N) and nozzle diameter (D_0) in the MCED process. The simulation results are validated with experimental data. Based on theoretical approach and experimental observation, the diameter of the deposited wire is in the range of 0.5–0.9 times of the nozzle diameter. The applicable range for v_N for various nozzle diameters is computed. The results showed that the contribution of migration flux to total flux remains nearly constant ($\sim 50\%$) for all values of pipette diameter in the range examined (100 nm–5 μm), whereas the contribution of diffusion and evaporation fluxes to total flux increase and decrease with the increasing pipette diameter, respectively. Results of this multiphysics study can be used to guide the experiment for optimal process conditions. *Published by AIP Publishing.* [<http://dx.doi.org/10.1063/1.4984910>]

I. INTRODUCTION

Three-dimensional (3D) printing in small scale has attracted significant interest within additive manufacturing community. Most low cost effective methods have been developed for printing plastic or polymers.^{1,2} New approaches have been recently established to print metals in nano/micro-scale, given potential applications in micro/nanoscale sensors and electronic devices.^{3–10} The common 3D printing processes for metals at macroscale such as laser sintering and electron beam melting processes are not suitable for micro-scale, given the size of the individual metal powders in the range of 20 μm –100 μm .¹¹ Meniscus-confined electrodeposition (MCED) is one of the 3D printing approaches that enables the fabrication of precise metallic micro/nanostructures in a cost-effective manner, using metal electrolytes at room temperature.^{4,12–15} In this method, electrodeposition (electroplating) is performed within a liquid meniscus between the tip of a pipette (often a glass capillary) and a conductive substrate. The metal deposition through the confined meniscus is a complex multi-physics process in which electrodeposition, fluid dynamics, mass, and heat transfer physics are simultaneously involved. Parameters such as relative humidity of the environment, size of the nozzle, speed of the nozzle, applied electric potential, and concentration of the electrolyte ultimately govern this micro/nanoscale additive manufacturing process.¹⁴ Given the multiphysics nature of the process, numerical simulation using multiphysics finite element (FE)

analysis is a suitable method to investigate the effect of process parameters on process outcomes. The effect of environmental relative humidity was studied in the earlier work of the authors.¹⁴ The results of that study revealed that flux of ions toward the cathode increased by lowering the relative humidity (RH) of the environment due to the increased evaporation rate from the meniscus surface. In addition, the evaporation process generated a convective flow in the nozzle that influenced the concentration of the ions at the cathode surface, which controls the deposition rate. In this work, we investigate the effect of nozzle speed (v_N) and nozzle diameter (D_0) on the process. A finite element (FE) model was developed to study the influence of nozzle speed and diameter on MCED. Four involved physics, i.e., electrodeposition, fluid dynamics, and mass and heat transfer, were considered. The FE results were validated by comparing to the experimental data. The applicable range for v_N was defined, and its influence on the transport mechanisms of the ions was elucidated.

II. MULTI-PHYSICS PROCESS

The schematic of the meniscus-confined 3D nano-printer and close-up view of the liquid meniscus are shown in Figs. 1(a) and 1(b), respectively. The printing process is based on localized electrodeposition at the tip of a glass pipette. Copper ions (Cu^{2+}) are reduced and deposited at the growth front of the wire as the pipette is moved upward. The involved physics are elaborated as follows.

Electrochemical dynamics of the electrolyte is described by the Nernst-Planck equation:

^{a)}Author to whom correspondence should be addressed: majid.minary@utdallas.edu

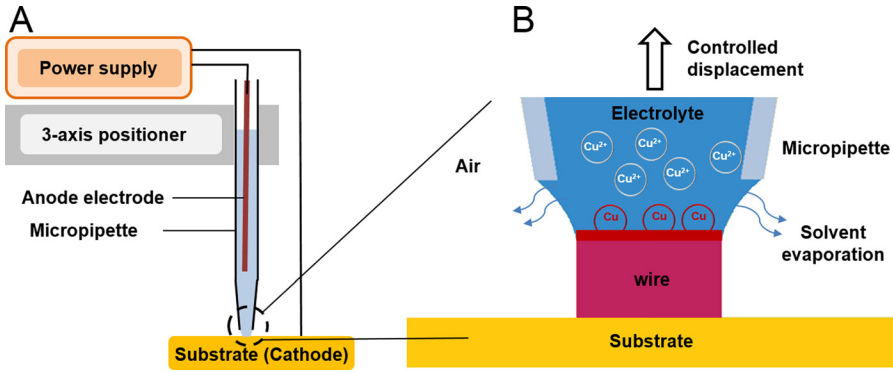


FIG. 1. (a) Schematic illustration of the 3D nano-printer. (b) Close-up view of the liquid meniscus between the pipette nozzle and the deposited wire.

$$N_i = -D_i \nabla c_i - z_i u_i F c_i \nabla \phi_l + c_i u, \quad (1)$$

in which N_i is the transport vector; the diffusivity of the ionic species is denoted by D_i ; concentration of the ion i , the electronic charge of the ionic species, and the mobility of the charged species are shown by c_i , z_i , and u_i , respectively. In Eq. (1), F is the Faraday constant; the electric potential difference in the electrolyte is shown by ϕ_l ; and u is the fluid velocity. Within the electrolyte, the ionic flux is governed by the first, second, and third terms in the Nernst-Planck equation corresponding to the diffusion, migration, and convection processes, respectively.¹⁶ Boundary conditions for the anode and the cathode are charge-transfer reaction kinetics defined by the Butler-Volmer expression. The charge transfer current or local current density (i_{ct}) on the electrode surface is expressed by

$$i_{ct} = i_0 \left\{ C_R \exp\left(\frac{\alpha_a F \eta}{RT}\right) - C_0 \exp\left(\frac{-\alpha_c F \eta}{RT}\right) \right\}, \quad (2)$$

where the exchange current density is i_0 ; the dimensionless concentration of the reduced species is C_R ; the dimensionless concentration of the oxidized species is C_0 ; the charge transfer coefficients for the anode and cathode are α_a and α_c , respectively, and η denotes the overpotential. The first and second terms in Eq. (2) represent the anodic and cathodic components of the local current density. During the deposition process, the wire growth front (cathode) moves in the vertical (growth direction). Steady-state growth of the wire is obtained when v_N is equal to the average growth rate of the

wire. In the FE model, it was assumed that the average wire growth rate is equal to the nozzle speed, since we aim to investigate the steady-state growth rate of the wire. Therefore, the nozzle speed v_N can be expressed by $v_N = -\frac{M_{Cu} i_{ct}}{z_{Cu} \rho_{Cu} F}$, where M_{Cu} is the molar mass, and ρ_{Cu} is the density of copper.^{16,17}

Solvent evaporation from the meniscus free surface has a significant effect on MCED.^{14,18} Heat and mass transfer physics must be taken into account to model evaporation from the electrolyte in the meniscus. Evaporation was simulated by using the diffusion equation for vapor concentration within the air domain. Water evaporation from the meniscus surface generates convective flow within the electrolyte domain, which was modeled by the Navier-Stokes together with the continuity equations.^{14,19}

III. FINITE ELEMENT MODELING

A. Geometry

Numerical simulations were conducted in COMSOL Multi-physics. A 2D axisymmetric finite element model was employed to simulate the process. The geometric detail of the FE model is shown in Fig. 2(a), which represents a micro-pipette filled with a liquid electrolyte of the metal of interest. In the experiment, we used CuSO_4 for printing Cu structures. Cylindrical coordinates were introduced with the z -axis in the vertical (nozzle) direction. Growth angle (φ_0) was defined as the angle between the line tangent to the meniscus and the wire axis. The growth angle was calculated to be $\sim 12^\circ$ for the copper-water-air system.^{4,14}

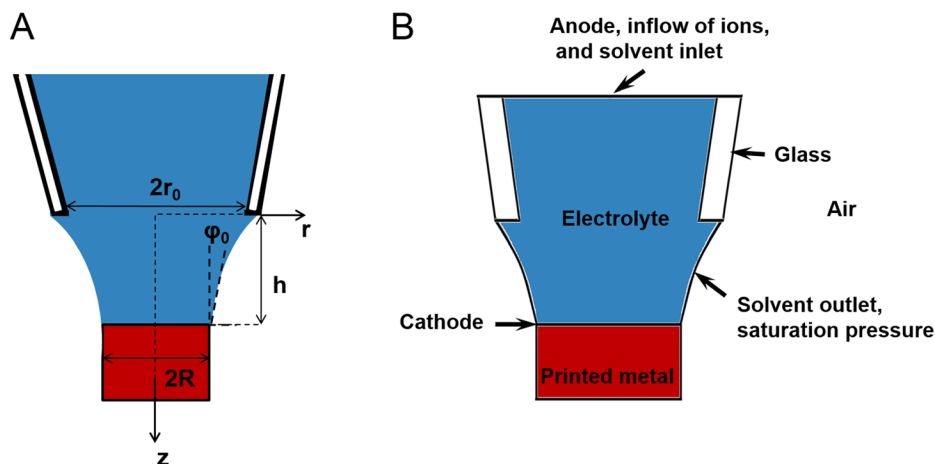


FIG. 2. (a) Details of the computational geometry and the coordinate system used to describe the liquid meniscus in the vertical wire deposition process. (b) Applied boundary conditions in the finite element model.

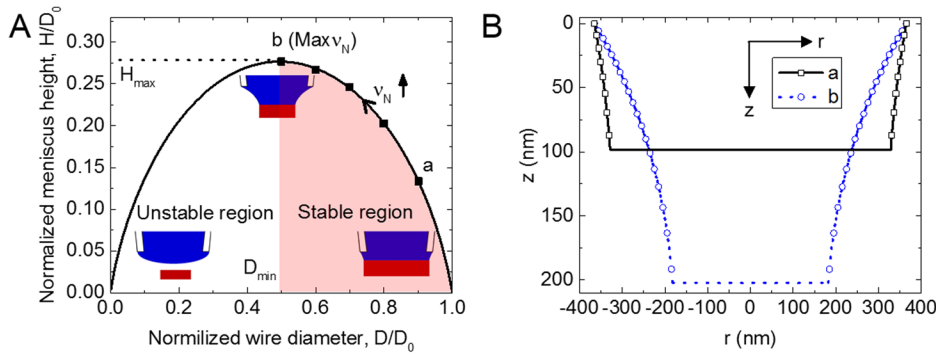


FIG. 3. (a) Normalized meniscus height vs. normalized wire diameter. (b) Meniscus profiles corresponding to points a and b in (a) for the pipette with the nozzle diameter of 730 nm.

The relation between the meniscus height and the diameter of the deposited wire for a given pipette is expressed as⁴

$$H(D) = \frac{1}{2}D \cos \varphi_0 \left(\cosh^{-1} \frac{D_0}{D \cos \varphi_0} - \cosh^{-1} \frac{1}{\cos \varphi_0} \right), \quad (3)$$

in which D and D_0 are diameters of the deposited wire and pipette nozzle, respectively; φ_0 denotes the growth angle, and H is the meniscus height. The normalized meniscus height versus normalized diameter of the deposited wire with respect to the nozzle diameter is plotted in Fig. 3(a). According to Eq. (3), the maximum height of the meniscus occurs at $H_{\max} = 0.28D_0$. This maximum height divides the curve in Fig. 3(a) into two regions: stable and unstable. By increasing v_N in the stable region, the liquid meniscus is stretched and meniscus height increases from zero up to the maximum meniscus height H_{\max} , whereas the diameter of the deposited wire reduces from the value near D_0 to the value of $D_{\min} = 0.5D_0$ [point b in Fig. 3(a)]. Only within this region, the meniscus is stable and a continuous wire deposition can be sustained. Any further increase in v_N shifts the meniscus height to the unstable region, which results in breakage of the liquid meniscus. Since the ionic current is essential for the continuous deposition, the breakage of the meniscus eliminates the ionic current and deposition stops.

It can be concluded that maximum value of v_N occurs at D_{\min} , which was also observed in the experiment. In this study, therefore, it is assumed that maximum v_N occurs at $D_{\min} = 0.5D_0$. It can be assumed that the minimum value of v_N happens at the points where $D_{\min} = D_0$ and $H = 0$. However, the largest value for the diameter of the wire in the experiments was $D_{\max} = 0.9D_0$ [point a in Fig. 3(a)]. At the points where $D > 0.9D_0$ ($H < 0.28D_0$), wire growth front easily reaches the pipette tip, and the deposited metal clogs the pipette due to the small height of the meniscus. Therefore, the minimum values of v_N was assumed to occur at $D_{\max} = 0.9D_0$ [point a in Fig. 3(a)]. Five different meniscus heights between points a to point b were chosen for the simulation [points shown in Fig. 3(a)]. In the coordinate system established in Fig. 2(a), the meniscus shape during stable growth is described by^{20,21}

$$z(r) = \frac{1}{2}D \cos \varphi_0 \left(\cosh^{-1} \frac{D_0}{D \cos \varphi_0} - \cosh^{-1} \frac{2r}{D \cos \varphi_0} \right). \quad (4)$$

As an example, the meniscus shape for points a and b in Fig. 3(a) for a micropipette with the nozzle diameter of $D_0 = 730$ nm are shown in Fig. 3(b). This pipette diameter was chosen from one of the experiments.

Changing the hydrophobicity of the substrate can affect the shape of the meniscus at the initial stage of deposition since the growth angle at the initial stage depends on the surface properties of the substrate. The electrolyte on a hydrophobic surface might exhibit a higher initial growth angle than on a hydrophilic surface, which will result in a larger base for the wire. In this work, however, the steady state wire growth is studied (away from the base), and the growth angle for the copper-water-air system (12°) was used in the simulation. As shown later in Fig. 4(b), the base of the wire is often larger than the steady state wire diameter. Also, the hydrophobicity of the nozzle surface may change the contact angle of the meniscus and the pipette.

Two-dimensional triangular elements with a maximum element size of 9 nm were used to construct the geometry. Mesh sensitivity analysis was carried out for the model with various mesh densities. Results of this analysis showed that good convergence was achieved for element size less than 9 nm. A total number of 51 213 elements was used in the simulation.

B. Boundary conditions

The system consists of electrolyte (copper ions (Cu^{2+}) and sulfate (SO_4^{2-}) in an aqueous solution), surrounding

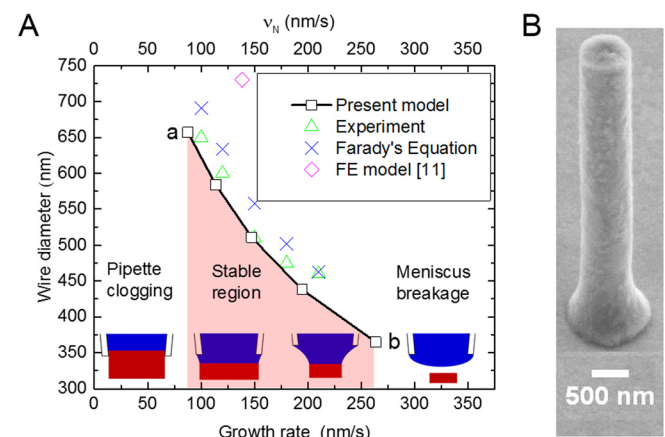


FIG. 4. (a) Dependence of the diameter of the deposited wire on v_N for the nozzle diameter of 730 nm. (b) An SEM image of a deposited wire.

environment (air), and the micro-pipette (glass). Ionic transport was modeled by utilizing the Nernst-Planck equation for the electrolyte coupled with the Navier-Stokes equation for the convective flow. The applied boundary conditions are shown in Fig. 2(b). Since the nozzle vertical walls are electrically insulated, the copper ion flux at these boundaries will be zero. Moreover, no slip condition was applied on the nozzle's internal wall. Steady-state growth of the wire was obtained when v_N was set equal to the average growth rate of the wire. The initial values and boundary conditions in the model were assigned based on the experimental conditions. Conditions included assuming atmospheric pressure and room temperature for all domains; and a bulk concentration of 10 mol/m^3 (0.01 mol/lit) for the electrolyte. A potential difference of 0.4 V was applied between the anode and the cathode. No heat source existed in the simulation, and the only heat transfer was due to evaporation of water from the meniscus surface. The diffusivity of the Cu^{2+} ions was assumed to be $5 \times 10^{-10} \text{ m}^2/\text{s}$.^{22,23} Electrolyte viscosity and density assumed to be $0.0010093 \text{ Pa}\cdot\text{s}$ and 1000 kg/m^3 , respectively. The values for the constants in Eq. (2) were $i_0 = 30 \frac{\text{A}}{\text{m}^2}$; $\alpha_a = 0.5$; $\alpha_c = 1.5$; $C_0 = \frac{C_{\text{Cu}^{2+}}}{C_{\text{Cu}^{2+},\text{ref}}}$; $C_R = 1$;^{17,24–26} where $C_{\text{Cu}^{2+}}$ and $C_{\text{Cu}^{2+},\text{ref}}$ are the concentration of Cu^{2+} ions on the electrode surface and in the bulk electrolyte, respectively.¹⁷

According to the author's earlier study¹⁴ and experimental results, an environmental relative humidity of 70% is the optimum condition for a stationary and stable wire growth. Therefore, all simulations were performed in this condition. A parametric study on the pipette length showed that the results were not affected when the length of the pipette was large enough in comparison with meniscus height. Therefore, the pipette length was set to be 100 times of the meniscus height.

Although electrodeposition is an exothermic process, the exchange of thermal energy in this process is not large compared to liquid-gas phase transformation. Therefore, in the present study, heat transfer happens only due the water evaporation from the meniscus free surface. Since no environmental change occurs during the electrodeposition given the controlled environment, the heat transfer process was considered as a time-independent process. A steady state wire growth was studied in this article. Therefore, any dynamic effects on the mass transfer of electrodeposition was neglected.

IV. RESULTS AND DISCUSSION

A. Validation of the computational model

The presented FE model was used to investigate the effect of the nozzle speed (v_N) on the MCED process. Five different heights of the meniscus within the stable region [points shown in the Fig. 3(a)] were considered for the analysis. Figure 4(a) shows the predicted values of v_N for the different shapes of the meniscus for a pipette with the nozzle diameter of 730 nm. The increase in v_N from 88 nm/s (minimum v_N) to 263 nm/s (maximum v_N) resulted in the decrease in wire diameter in the stable region from 657 nm to 365 nm [from point *a* to point *b* Fig. 3(a)]. In order to validate the FE

simulation, different v_N values within the predicted stable range were used in the experiments. The diameter of the deposited wire at each v_N was measured using SEM micrographs. As an example, the SEM image of a deposited wire is shown in Fig. 4(b). The experimental data for the pipette with the nozzle diameter of 730 nm are also shown in Fig. 4(a). Numerical results showed good agreement with the experimental data. Increasing v_N stretches the meniscus and decreases the diameter of deposited wire from the point *a* to point *b* shown in Fig. 3(a). Experimental data revealed that by increasing v_N from 100 nm/s to 210 nm/s, the wire diameter decreased from 650 nm to 460 nm, respectively. Experimental observation also showed that for v_N approaching $\sim 270 \text{ nm/s}$ (point *b*) the meniscus broke due to liquid instability, and for v_N lower than $\sim 100 \text{ nm/s}$ (point *a*), the pipette frequently clogged. The clogging of the pipette for slow v_N was because the meniscus height became very small and the wire growth front reached the pipette nozzle.

Additionally, Faraday's equation can also be used to predict the wire diameter (D),⁴ $D = \sqrt{\frac{iM}{nF\rho\pi v_N}}$, where i and v_N are the experimental values for the ionic current and nozzle withdrawal speed, presented in Table I; F is the Faraday constant; M and ρ are the molar mass and the density of copper, respectively; and for Cu^{2+} , $n=2$. In other words, $D \propto \sqrt{i/v_N}$. The predicted values using Faraday's equation for the diameter of the deposited wire is also shown in Fig. 4(a). The analytical results showed reasonable agreement with the experimental values, and FE simulation results. Included in the Fig. 4(a) is also the numerical result using the earlier finite element model presented by Seol *et al.*¹⁸ In their study, a cylindrical geometry was assumed for the meniscus ($\varphi_0 = 0$), and the wire diameter and meniscus height were equal to 1 and 0.75 times of the nozzle diameter, respectively. The assumed meniscus height was 2.7 times larger than H_{max} calculated by Eq. (3). Comparison to the experimental data, the predicted value for v_N in this case does not show good agreement. Therefore, considering the realistic geometry of the liquid meniscus is essential to obtain accurate results from the FE model.

B. Effect of the nozzle speed on MCED

The nozzle speed v_N affects the MCED process through two mechanisms. First, it directly influences the electrodeposition process by adjusting the diameter of the deposited wire (cathode). Changes in the wire diameter influence the amount of ions deposited on the wire growth front and affect the concentration of Cu^{2+} ions within the electrolyte. Second, v_N affects evaporation on the meniscus surface by changing the meniscus profile. Evaporation was established to be one of the key factors governing the MCED process, since it

TABLE I. Electrical current and v_N in the experiment for the nozzle with the diameter of 730 nm.

v_N (nm/s)	100	120	150	180	210
Current (nA)	1.02	1.03	1.00	0.97	0.96

controls the flux within the electrolyte.¹⁴ The evaporation rate along the meniscus free surface [denoted by the x-coordinate in the inset of Fig. 5(a)] for the two extreme predicted values of v_N i.e., 88 nm/s and 263 nm/s is depicted in Fig. 5(a). The results show that water evaporates faster at the top and bottom corners of the meniscus since the evaporation rate is higher at solid/liquid contact line, and it is uniform away from the corners.^{14,27} Increasing v_N stretches the meniscus, so the meniscus height for $v_N = 263$ nm/s becomes 2.06 times of the one at $v_N = 88$ nm/s [Fig. 3(b)].

We define the volumetric evaporation (VE) as the amount of water evaporated per second from the meniscus, which can be calculated by $VE = AER \times A$, where A is the

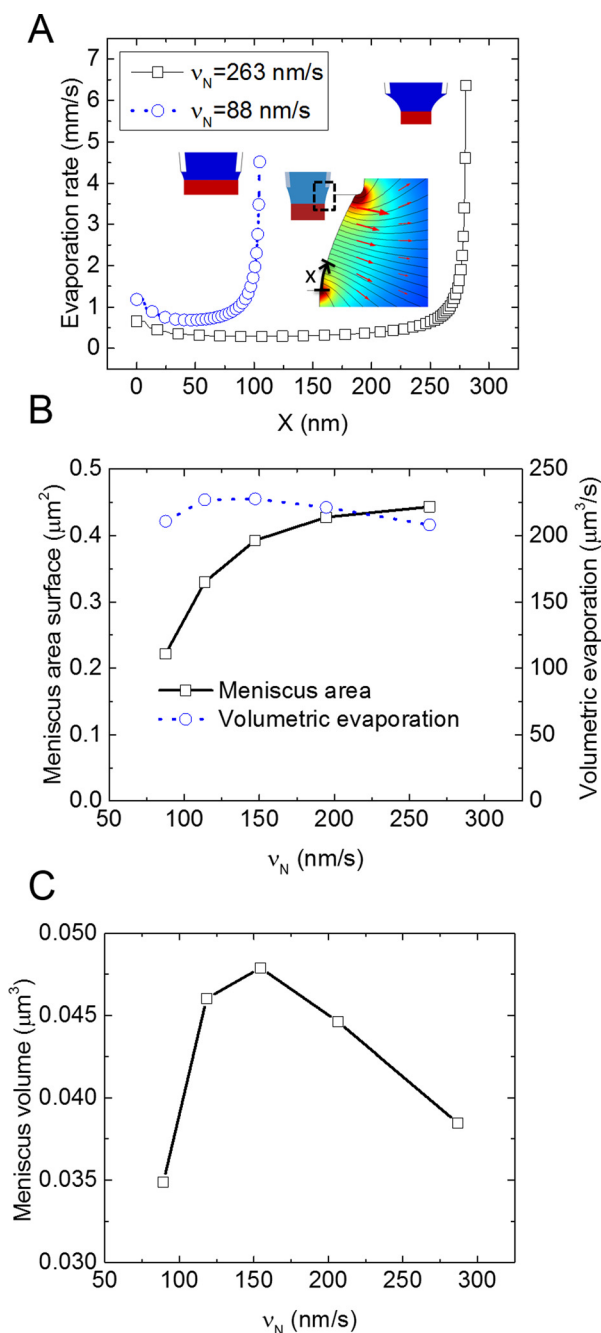


FIG. 5. (a) Profiles of evaporation rate along the meniscus surface for v_N of 263 and 88 nm/s, (b) meniscus surface area and volumetric evaporation vs. v_N , and (c) volume of the meniscus vs. v_N .

area of the meniscus surface, and AER is defined as the average evaporation rate along the meniscus. Figure 5(b) shows the meniscus surface area and the volumetric evaporation vs. v_N . The surface area of the meniscus monotonically increases with v_N , whereas the volumetric evaporation rate is nearly constant for all v_N , with slight variation. Figure 5(c) shows the volume of the meniscus vs. v_N , which shows the increase with v_N up to ~ 150 nm/s and then decreases for higher v_N .

AER and average concentration of Cu^{2+} ions vs. v_N are shown in Fig. 6(a). AER along the meniscus for $v_N = 88$ nm/s was 0.95 mm/s, which is roughly twice the value for the $v_N = 263$ nm/s. The values of VE were 2.11×10^{-16} m^3/s and 2.08×10^{-16} m^3/s for the v_N of 88 nm/s and 263 nm/s, respectively. Even though the AER highly depends on v_N , VE is nearly constant for the all v_N [Fig. 5(b)]. As can be seen in Fig. 6(a), the concentration of ions within meniscus increases by increasing v_N . At higher v_N , meniscus stretches, and the radius of the deposited wire decreases, so fewer ions are reduced (consumed) at the wire growth front. As a result, the concentration of ions within the meniscus considerably increases with v_N . In the MCED process, ions are transported between the anode and cathode electrodes through convection, diffusion, and migration processes, simultaneously [Eq. (1)]. Evaporation stimulates the convective flux within

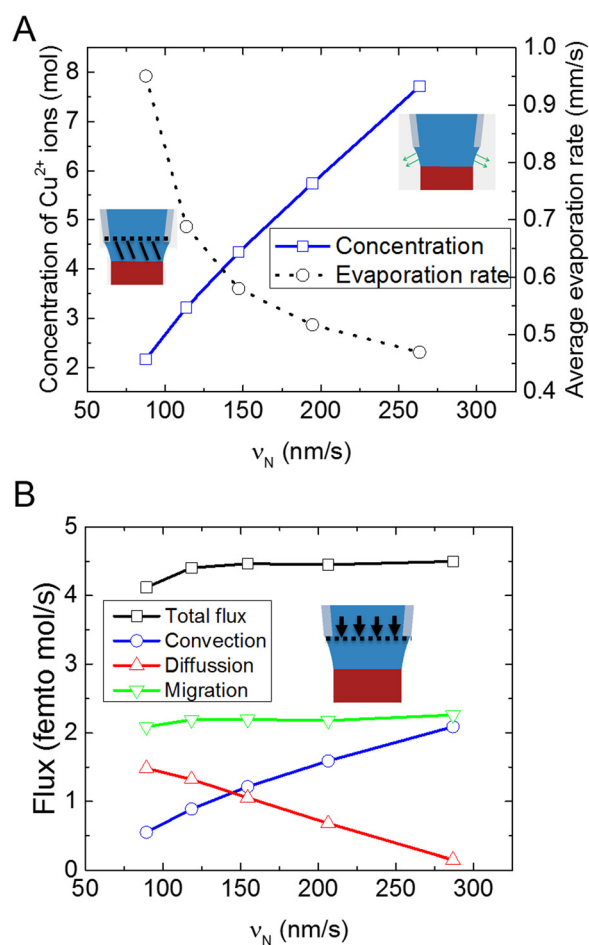


FIG. 6. (a) Average concentration of Cu^{2+} ions within the meniscus and average evaporation rate at the meniscus surface vs. v_N . (b) Flux of Cu^{2+} ions that exit nozzle vs. v_N . Total flux, as well as convection, diffusion, and migration fluxes are shown.

the electrolyte and brings the ions from the bulk electrolyte toward the meniscus' surface. The diffusion flux and migration flux are generated due to the ion concentration gradient and applied electric potential, respectively. The total ionic flux between the nozzle tip and the meniscus, as well as convection, diffusion, and migration fluxes vs. v_N , is shown in Fig. 6(b). According to the third term in Eq. (1), convective flux ($c_i u$) depends on both the flow velocity within the electrolyte (u) generated due to evaporation at the meniscus surface (VE) and the concentration of the ions (c_i). Although VE is almost constant for all v_N [Fig. 5(b)], the concentration of ions (c_i) increases at higher v_N [Fig. 6(a)]. Therefore, increasing v_N increases the magnitude of the convective flux. The magnitudes of convective flux for the v_N of 263 nm/s is 20.9×10^{-15} mol/s, which is ~ 3.8 times the value for 88 nm/s. The diffusion flux depends on the concentration gradient. The lower concentration gradient between the meniscus and bulk electrolyte reduces diffusion flux at high v_N [Fig. 6(a)]. Since diffusion and convection are reversely affected by the Cu^{2+} ions concentration, their contribution to the total flux remains nearly constant for all values of v_N . Contribution of convection and diffusion together to total flux is $\sim 50\%$. The contribution of convection is $\sim 13.3\%$ and 46.4% , whereas the contribution of the diffusion is 36% and 3.3% at $v_N = 88$ nm/s and 263 nm/s, respectively. The magnitude of the migration flux was calculated to be $\sim 2.2 \times 10^{-15}$ mol/s, which is $\sim 50\%$ of total flux. The magnitude of the total flux were calculated to be 4.12×10^{-15} mol/s and 4.5×10^{-15} mol/s for the v_N of 88 nm/s and 263 nm/s, respectively.

The concentration and flux map of Cu^{2+} ions for $v_N = 88$ nm/s and 263 nm/s are shown in Fig. 7. As it was expected, the concentration of Cu^{2+} ions was higher at $v_N = 263$ nm/s. The convection flux within the electrolyte is shown in the Fig. 7(b). The results showed that higher convection was generated on the meniscus top corner because the evaporation rate was higher in that region [Fig. 5(a)]. Convection carries the Cu^{2+} ions to the meniscus surface and generates a diverging flux that increases the concentration at the vicinity of meniscus free surface [Fig. 7(a)]. Diffusion carries the ions from the electrolyte bulk and meniscus surface toward wire growth front due to concentration gradient and facilitates more uniform concentration distribution, which results in a converging ion flux [Fig. 7(c)]. At $v_N = 263$ nm/s, however, back diffusion happens since the concentration of Cu^{2+} ions in the meniscus top corner is higher than the bulk solution [Fig. 7(a)]. At $v_N = 88$ nm/s, all the ions brought by convection and migration are consumed by electrodeposition, because the electrodeposition consumes more ions since the cross-section of the wire (cathode surface) is 1.8 times larger than $v_N = 263$ nm/s. Therefore, the concentration of Cu^{2+} ions within the meniscus remains considerably less than the bulk electrolyte, which triggers the diffusion to bring the ions from the electrolyte bulk to the wire growth front. Migration and diffusion are the dominant flux transport mechanisms near the wire growth front [Figs. 7(c) and 7(d)]. The direction of total flux [Fig. 7(e)] is from bulk electrolyte to the wire growth front and has its highest value close to the center-line of the

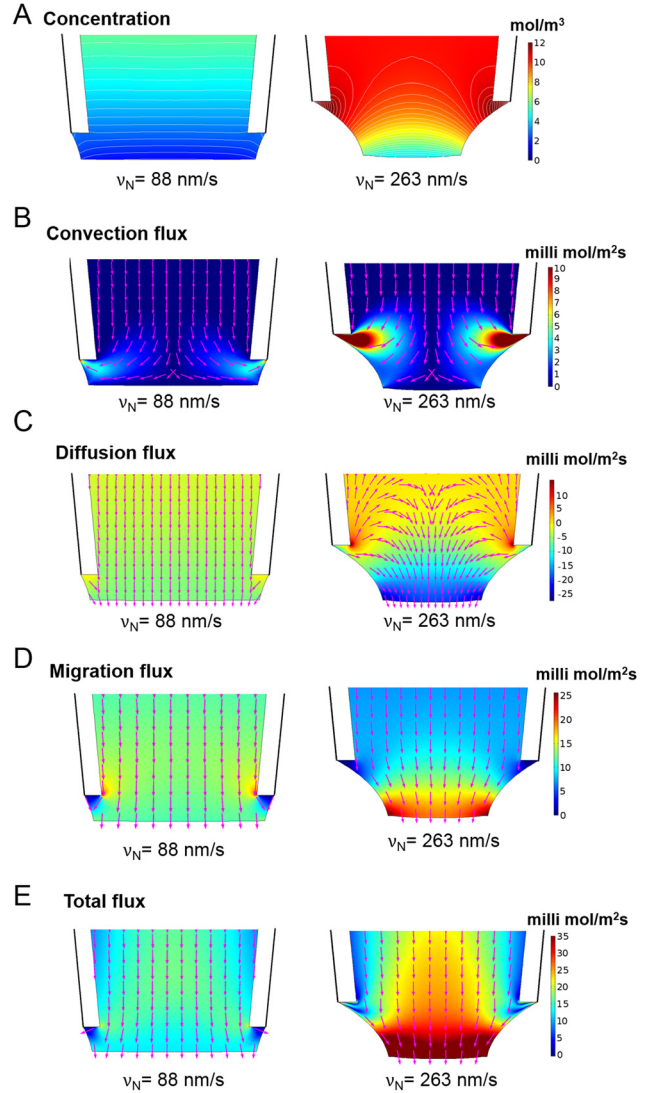


FIG. 7. (a) Concentration distribution of Cu^{2+} ions in electrolyte. Graphical representation of flux map of ions close to the wire growth front, illustrating (b) convection flux, (c) diffusion flux, (d) migration flux, and (e) total flux for the nozzle with v_N of 88 nm/s and 263 nm/s. The diameter of the nozzle is 730 nm in this simulation.

meniscus, in particular near wire growth front, due to the contribution of migration and diffusion.

Due to strong diverging convective flux at higher v_N [Fig. 7(b)], the concentration of Cu^{2+} ions at the wire edge gets higher than the wire center [Fig. 7(a)]. The resulting increase in the concentration would increase the growth rate at the wire edge according to Eqs. (2) and (3). The concentration (C) and growth rate (GR) ratio between the edge (e) and the center (c) of the wire for different values of v_N are compared in Table II. The value of growth rate ratio exceeds 1.94 at $v_N = 263$ nm/s, which might cause deposition of

TABLE II. Concentration and growth rate ratio for different v_N . C and GR are concentration and growth rate, respectively.

v_N (nm/s)	88	114	147	195	263
C_e/C_c	1.21	1.35	1.42	1.50	1.71
GR_e/GR_c	1.19	1.40	1.51	1.63	1.94

hollow structures for higher v_N .¹⁴ The $v_N = 263$ nm/s could not be applied in the experiment due to meniscus instability on the hollow structures. The results show that if fabrication of hollow structures is desired, higher v_N should be used.

C. Effect of the nozzle diameter on MCED

A parametric study was carried out to investigate the influence of the nozzle diameter on MCED. The diameter of the nozzle was varied in the desired range of experimental values for nozzle diameter, from 100 nm to 5 μ m, which is relevant for micro/nanoscale 3D printing. For a given nozzle diameter, v_N can vary from the minimum to maximum value corresponding to the minimum ($D_{min} = 0.5 D_0$) and maximum ($D_{max} = 0.9 D_0$) permissible deposited wire diameters, respectively [points *a* and *b* in Fig. 3(a)]. The total flux of Cu^{2+} ions that exits the nozzle vs. nozzle diameter is shown in Fig. 8(a). The total flux is roughly independent from v_N , while it has linear relation with nozzle diameter. Note that the x-axis is in the logarithmic scale. By increasing the number of Cu^{2+} ions carried to meniscus, the ionic current is expected to increase. The predicted ionic current as a function of nozzle diameter is shown in Fig. 8(b). Similar to total flux, ionic current linearly increases with the nozzle diameter with the slope of ~ 0.0012 nA/nm. Ionic current can be measured in the experiment by monitoring the current in the circuit between the anode and the cathode.

Two experimental data points for the pipette with a nozzle diameter of 730 nm for different values of v_N are added in the Fig. 8(b). The measured values of electrical current in experiment for the v_N of 100 nm/s and 210 nm/s were 1.02 nA and 0.96 nA, respectively. Similar to FE results, experiment data show that ionic current does not strongly depend on v_N as long as the chosen v_N lies within its applicable range. The applicable range of v_N for different nozzle diameters is shown in Fig. 8(c). The applicable range for v_N highly depends on the nozzle diameter. The value of applicable v_N increases with decreasing diameter of the nozzle. The results show that the deposition rate for a pipette of 100 nm in diameter can be in the range of 524 nm/s–2.3 μ m/s, while the deposition rate decreases to 14.5 nm/s–45 nm/s for a pipette of 5 μ m in diameter.

The contribution of the three ionic fluxes to the total flux that exit the nozzle tip for the minimum v_N and maximum v_N are shown in Figs. 9(a) and 9(b), respectively. The contribution of the migration is approximately 50% of the total flux and does not strongly depend on v_N or nozzle diameter. However, diffusive flux and convective flux are different for minimum v_N [Fig. 9(a)] and maximum v_N [Fig. 9(b)]. The graphs can be roughly divided into two regions: $D > 2$ μ m and $D < 2$ μ m. The total contributions of convection and diffusion remains $\sim 50\%$ for all v_N . For large pipettes with the nozzle diameters over ~ 2 μ m, the contribution of convection flux is $\sim 35\%$ and $\sim 9\%$ for the maximum and minimum v_N , and does not depend on the nozzle diameter. It can be concluded that wire with uniform cross-section can be deposited in large pipettes since convection contribution is not high. The contribution of diffusion and convection is almost constant for large pipettes. The values of convection

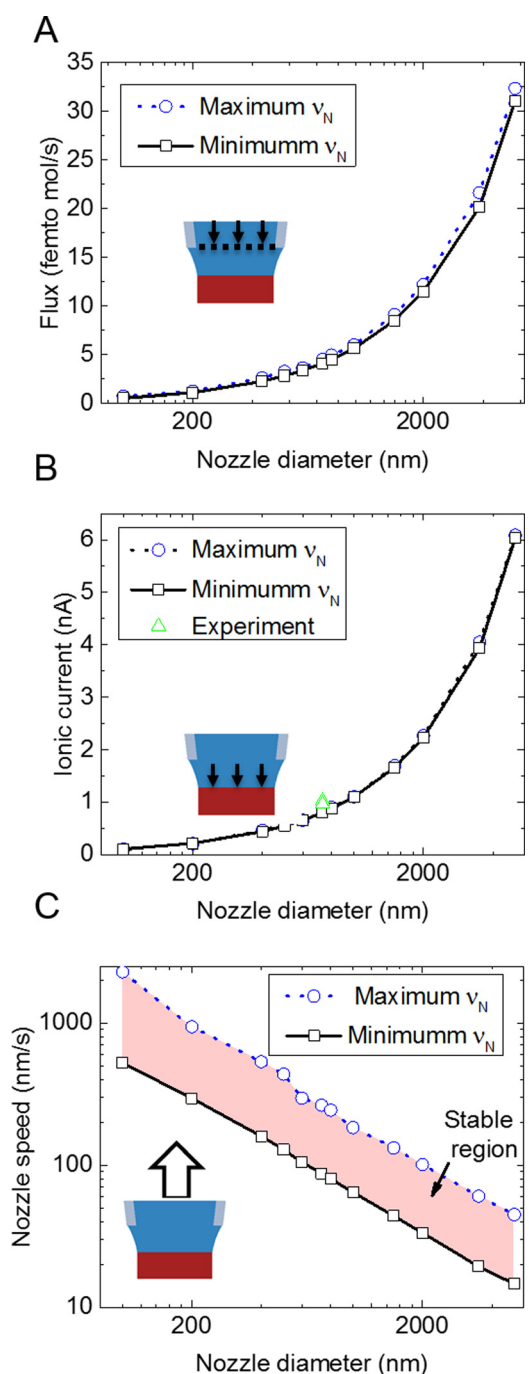


FIG. 8. Effect of nozzle diameter on (a) total flux of Cu^{2+} ions that exit the pipette nozzle, (b) ionic current, and (c) minimum and maximum permissible values for v_N . In C, both axes are in logarithmic scale. In (a) and (b), the x-axis is in the logarithmic scale.

and diffusion contributions are 9% and 41% for minimum v_N , and 34% and 16% for maximum v_N , respectively.

For pipettes with the nozzle diameter smaller than ~ 2 μ m, the contribution of convection and diffusion varies with the diameter of the nozzle. For minimum v_N , all fluxes are toward the growth front; however, for maximum v_N , back diffusion happens in certain regions of the pipette (pipettes with the nozzle diameter smaller than 730 nm). In this case, convection takes a larger contribution in the total flux. In addition, in this case, the contribution of convection becomes even larger than migration. For pipette with nozzle

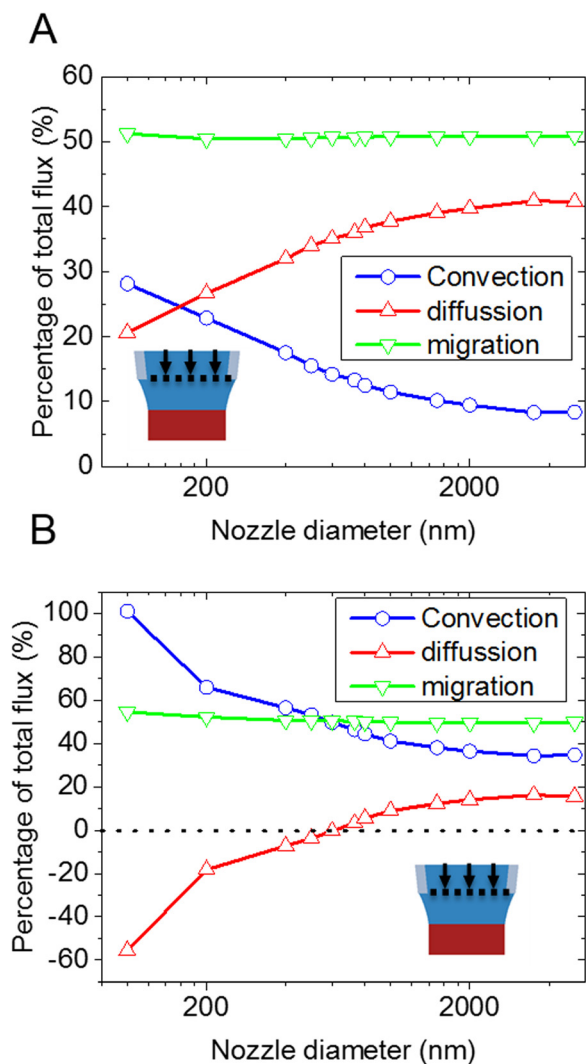


FIG. 9. Contribution of each transport mechanisms for (a) minimum v_N , and (b) maximum v_N . X-axis is in the logarithmic scale.

diameter of 100 nm, contribution of convection is over 100% of the total flux, which reveals the importance of evaporation in the small pipette range for high v_N . The large convection flux in small pipettes is due to the high Cu^{2+} ions concentration and high evaporation rate.

Figure 10(a) shows the average evaporation rate at the meniscus free surface as a function of nozzle diameter for minimum and maximum of v_N , respectively. The evaporation rate increases as the nozzle diameter decreases. For example, the average value of evaporation rate for a pipette with a nozzle diameter of 100 nm is ~ 47 times larger than the pipette with the nozzle diameter of 5000 nm for both cases of minimum and maximum v_N , which shows the importance of evaporation in the MCED process, in particular for small pipettes. This high value for evaporation rate in the small pipette is mainly due to the high surface area to volume ratio (A/V) of the meniscus.¹⁴ The A/V ratio for the pipette with the nozzle diameter of 100 nm is 50 times larger the pipette with a nozzle diameter of 5000 nm. Figure 10(b) shows the average concentration of ions within the meniscus as a function of nozzle diameter for minimum and maximum of v_N . For minimum v_N , concentration of electrolyte always remains below the

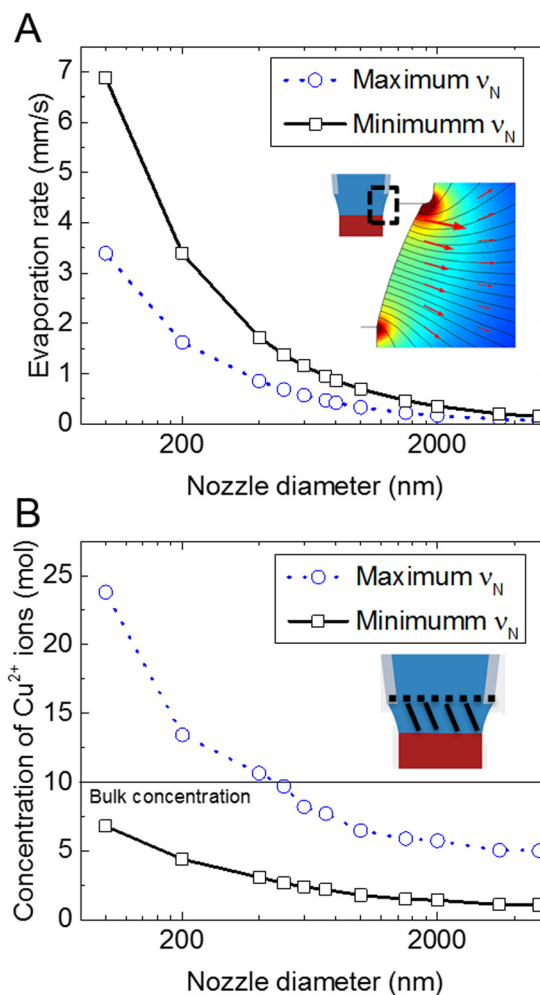


FIG. 10. (a) Average evaporation rate on the meniscus surface, and (b) average concentration of Cu^{2+} ions in the meniscus. X-axis is in the logarithmic scale.

concentration of bulk electrolyte. However, for maximum v_N , concentration of ions in meniscus becomes larger than bulk electrolyte for pipettes with the nozzle diameter less than ~ 500 nm. In this case, back diffusion from meniscus to the bulk electrolyte will happen.

Figure 11(a) shows the volumetric deposition rate ($\mu m^3/s$) vs. nozzle diameter. The volumetric deposition rate provides the volume rate of the deposited metal structure and was calculated by multiplying the linear deposition rate along the nozzle axis with the area of the deposited structure. This graph shows that larger pipettes can generate larger volumes of deposit, although the linear deposition rate for larger pipettes is much slower than the smaller pipettes [Fig. 8(c)]. Based on Fig. 10(a), the evaporation rate for small pipettes is much larger than the larger pipettes. Meanwhile, based on Fig. 8(c), the deposition rate for small pipettes is also higher than the large pipettes. Figure 11(b) shows the ratio of deposition rate/evaporation rate vs. nozzle diameter, for maximum and minimum v_N . As it turns out, this ratio is nearly constant for all nozzle diameters, which means that MCED is a process primarily driven by evaporation. The applicable range of v_N highly depends on the nozzle diameter [Fig. 8(c)]. This is due to the fact that evaporation is very

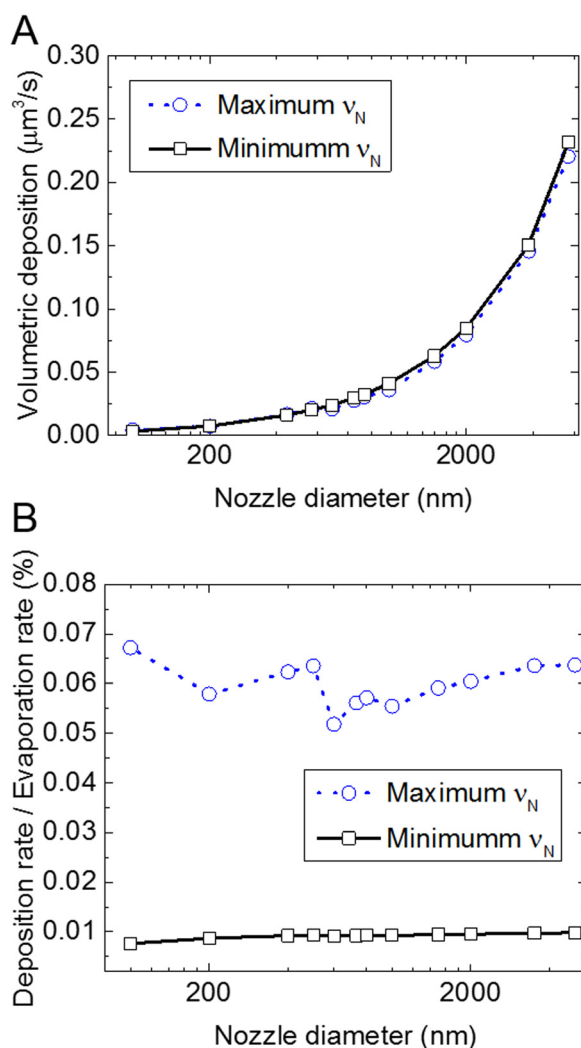


FIG. 11. (a) Volumetric deposition ($\mu\text{m}^3/\text{s}$) vs. nozzle diameter (nm). (b) Ratio of deposition rate/evaporation rate vs. nozzle diameter.

high and greatly depends on the meniscus shape for the small pipettes [Fig. 10(a)]. For the nozzle diameter of 100 nm, the average evaporation rate along the meniscus surface varies from 3.4 mm/s to 6.9 mm/s happening for the two extreme stable shapes of the meniscus [Fig. 10(a)]. The variation of evaporation rate in the small pipette highly affects the flux map (Fig. 9), concentration of Cu^{2+} ion [Fig. 10(b)], and deposition rate which is assumed to be equal to v_N [Fig. 8(c)]. The applicable range of v_N for the pipette with the nozzle diameter of 100 nm is predicted to be from ~ 520 nm/s to $2.3 \mu\text{m}/\text{s}$.

V. CONCLUSIONS

In summary, a multiphysics FE model was developed to investigate the influence of nozzle speed (v_N) and nozzle diameter on MCED. Based on theoretical approach and experimental observation, the diameter of the deposited wire are in the range of 0.5 – 0.9 times of the nozzle diameter. The computational model reveals that v_N influences the shape of the liquid meniscus between the tip of the nozzle and the growth front, and beyond a certain range, meniscus becomes unstable and breaks, which stops the deposition

process. In addition, the applicable range v_N for various nozzle diameters was computed. Within the stable range of v_N , diameter of the deposited structure decreases as the v_N increases. For example, for a pipette with the nozzle diameter of 730 nm, the increase in v_N from 88 nm/s (minimum v_N) to 263 nm/s (maximum v_N) resulted in decrease in wire diameter in the stable region from 657 nm to 365 nm. By increasing v_N , the surface area of the meniscus increases, and hence the average evaporation rate (mm/s) decreases. The volumetric evaporation rate ($\mu\text{m}^3/\text{s}$) remains nearly constant (~ 0.4 – $0.5 \mu\text{m}^3/\text{s}$) for all v_N . In addition, by increasing v_N concentration of ions within the meniscus increases, which is due to low consumption of metal ions for small diameter of the deposited structure under high v_N . As a result, by increasing v_N , contribution of diffusion flux to total flux decreases, and contribution of convection to the total flux increases. Contribution of migration to total flux remains nearly constant for all range of the v_N . The results show that the deposition rate decreases by increasing the nozzle diameter. For example, the deposition rate for a pipette of 100 nm in diameter can be in the range of ~ 520 nm/s– $2.3 \mu\text{m}/\text{s}$, whereas the deposition rate decreases to ~ 15 nm/s– 45 nm/s for a pipette of $5 \mu\text{m}$ in diameter. Contribution of migration to total flux remains nearly constant ($\sim 50\%$) for all values of pipette diameter in the range examined (100 nm– $5 \mu\text{m}$), whereas contribution of diffusion and evaporation fluxes to total flux increase and decrease with the increasing pipette diameter, respectively. The results also show that the evaporation rate decreases (from 3.5 to 7 mm/s to nearly zero) with increasing the nozzle diameter. Considering the deposition rate, the ratio of deposition rate/evaporation rate remains nearly constant for all nozzle diameters. This value was found to be ~ 0.01 and ~ 0.06 for minimum and maximum allowable nozzle speeds. We believe that results of this work can be used for optimization of the fabrication process in the experiment, which may in turn result in better mechanical and electrical properties of the fabricated structures.

ACKNOWLEDGMENTS

This work was supported by the U.S. Office of Naval Research under Young Investigator Program (Award No. N00014-15-1-2795).

- ¹B. J. de Gans, P. C. Duineveld, and U. S. Schubert, "Inkjet printing of polymers: State of the art and future developments," *Adv. Mater.* **16**(3), 203–213 (2004).
- ²P. Calvert, "Freeforming of polymers," *Curr. Opin. Solid State Mater. Sci.* **3**(6), 585–588 (1998).
- ³L. Hirt *et al.*, "Additive manufacturing of metal structures at the micrometer scale," *Adv. Mater.* **29**(17), 1604211 (2017).
- ⁴J. Hu and M.-F. Yu, "Meniscus-confined three-dimensional electrodeposition for direct writing of wire bonds," *Science* **329**(5989), 313 (2010).
- ⁵X. Zheng *et al.*, "Ultralight, ultrastiff mechanical metamaterials," *Science* **344**(6190), 1373–1377 (2014).
- ⁶L. Hirt *et al.*, "Template-Free 3D microprinting of metals using a force-controlled nanopipette for layer-by-layer electrodeposition," *Adv. Mater.* **28**(12), 2311–2315 (2016).
- ⁷J. S. Fisher *et al.*, "Rapid electron beam writing of topologically complex 3D nanostructures using liquid phase precursor," *Nano Lett.* **15**(12), 8385–8391 (2015).

- ⁸J. D. Whitaker, J. B. Nelson, and D. T. Schwartz, "Electrochemical printing: Software reconfigurable electrochemical microfabrication," *J. Micromech. Microeng.* **15**(8), 1498–1503 (2005).
- ⁹C. Ladd *et al.*, "3D Printing of free standing liquid metal microstructures," *Adv. Mater.* **25**(36), 5081–5085 (2013).
- ¹⁰B. Y. Ahn *et al.*, "Omnidirectional printing of flexible, stretchable, and spanning silver microelectrodes," *Science* **323**(5921), 1590–1593 (2009).
- ¹¹W. E. Frazier, "Metal additive manufacturing: A review," *J. Mater. Eng. Perform.* **23**(6), 1917–1928 (2014).
- ¹²P. S. Abhijit and Y. Min-Feng, "Electrochemical fountain pen nanofabrication of vertically grown platinum nanowires," *Nanotechnology* **18**(10), 105305 (2007).
- ¹³A. P. Suryavanshi and M.-F. Yu, "Probe-based electrochemical fabrication of freestanding Cu nanowire array," *Appl. Phys. Lett.* **88**(8), 083103 (2006).
- ¹⁴S. Morsali *et al.*, "Multi-physics simulation of metal printing at micro/nanoscale using meniscus-confined electrodeposition: Effect of environmental humidity," *J. Appl. Phys.* **121**(2), 024903 (2017).
- ¹⁵J. Hu *et al.*, "Diffusion limited current in very high aspect ratio Pt needle electrodes," *Appl. Phys. Lett.* **99**(5), 053113 (2011).
- ¹⁶H. Xiao *et al.*, "Three-dimensional microfabrication of copper column by localized electrochemical deposition," in *2016 17th International Conference on Electronic Packaging Technology (ICEPT)* (IEEE, 2016).
- ¹⁷D. R. Turner and G. R. Johnson, "The effect of some addition agents on the kinetics of copper electrodeposition from a sulfate solution: I. Cathode potential-current density relation," *J. Electrochem. Soc.* **109**(9), 798–804 (1962).
- ¹⁸S. K. Seol *et al.*, "Electrodeposition-based 3D printing of metallic micro-architectures with controlled internal structures," *Small* **11**(32), 3896–3902 (2015).
- ¹⁹Q. Sun *et al.*, "Micromechanical analysis of fiber and titanium matrix interface by shear lag method," *Composites, Part B* **79**, 466–475 (2015).
- ²⁰V. A. Tatarchenko *et al.*, "Theoretical model of crystal growth shaping process," *J. Crystal Growth* **180**(3), 615–626 (1997).
- ²¹V. A. Tatarchenko, *Shaped Crystal Growth* (Springer Netherlands, 2013).
- ²²J. T. Hinatsu and F. R. Foulkes, "Diffusion coefficients for copper (II) in aqueous cupric sulfate-sulfuric acid solutions," *J. Electrochem. Soc.* **136**(1), 125–132 (1989).
- ²³T. Hayashi *et al.*, "Role of cuprous ion in copper electrodeposition acceleration," *J. Electrochem. Soc.* **162**(6), D199–D203 (2015).
- ²⁴T. Braun and D. Schwartz, "Localized electrodeposition and patterning using bipolar electrochemistry," *J. Electrochem. Soc.* **162**(4), D180–D185 (2015).
- ²⁵E. Mattsson and J. O. M. Bockris, "Galvanostatic studies of the kinetics of deposition and dissolution in the copper + copper sulphate system," *Trans. Faraday Soc.* **55**(0), 1586–1601 (1959).
- ²⁶W. Zeng, M. L. Free, and S. Wang, "Simulation study of electrolyte flow and slime particle transport in a newly designed copper electrorefining cell," *ECS Trans.* **72**(22), 23–42 (2016).
- ²⁷M. A. Hampton *et al.*, "Influence of surface orientation on the organization of nanoparticles in drying nanofluid droplets," *J. Colloid Interface Sci.* **377**(1), 456–462 (2012).